Timelike Compton Scattering in the GlueX Experiment at Jefferson Lab

A thesis submitted in partial fulfillment of the requirement

for the degree of Bachelor of Science with Honors in Physics from

The College of William and Mary in Virginia,

by

Alexandra Gray Cramer

Accepted for Honors

(Honors or no-Honors)

Dr. Justin Stevens, Research Advisor

Dr. Irina Novikova, Senior Research Coordinator

Dr. Heather Sasinowska, Mathematics

Williamsburg, Virginia

May 4, 2018

Table of Contents

List of Figures

Glossary of Terms:

Calorimeter: cylindrical apparatus (within GlueX detector) that collects energy of particles from an electromagnetic shower in sections called modules (shower shape helps to identify particle types)

CEBAF: Continuous Electron Beam Accelerator Facility; located at Jefferson Lab in Newport News, Virginia; accelerates electrons to high energies to produce reactions due to collisions with a target

CDC (Central Drift Chamber): cylindrical apparatus (within GlueX detector) made up of many thin 'straw' (metal) tubes; tracks the position of charged particles using the locations of induced electric signal caused by passing particles

Compton Scattering: inelastic collision (kinetic energy is not conserved) of a photon and a charged particle (e.g. a proton)

Cross Section (particle physics): the likelihood that an initial particle scatters against a target, producing particles

DSelector: A ROOT programming class that is specific to the GlueX project (inherits from ROOT's TSelector); used to create data histograms

Feynman Diagram: A time (x) vs space (y) diagram of a sub-atomic particle reaction

Four-Momentum: A vector describing a particle's momentum in spacetime; contains E/c and the x,y,z directions; used for relativistic (near light speed) motion calculations

Gluon: massless particles that bind quarks, the fundamental particles that make up baryons (such as protons), together

GPD (Generalized Parton Distribution): three dimensional mathematical models in a momenta and position space used to describe the proton structure; experimental data can be used to draw comparisons between physical reactions and GPD theory calculations

J/ψ: a meson which decays into an electron and a positron; products identical to those of TCS

Meson: particle made up of one quark and one antiquark (which has quark properties but opposite sign); unstable and quickly decays into other particles (e.g. electron)

Preshower: energy collected in the first (innermost) layer of calorimeter modules; often used in ratio with energy deposited in subsequent layers to determine particle type

ROOT: an object-oriented programming language that is commonly used in particle physics

Run: An event-recording, data-collecting period (often ~ 2 hours) during which reactions occur in a detector, each typically containing ~ 100 million collision events in this experiment

Shower (e.g. electromagnetic shower): a stream or chain reaction of secondary particles (products formed from a reaction); shower properties examined within a detector (e.g. BCAL)

Timelike: Events involving real (nonvirtual) particles which can transform to a reference frame where they occur at the same place at different times; represented by spacetime 4-vector (x,y,z,ct) where $S^2 > 0$. Term in 'Timelike' Compton Scattering to contrast with inverse reaction Deeply Virtual Compton Scattering (DVCS)

Abstract

The structure of protons is a point of interest in nuclear physics due to the lack of consensus between the cumulative spin of a proton and the sum of the spins of its constituent quarks. In the GlueX Experiment at the Jefferson Lab Continuous Electron Beam Accelerator Facility (CEBAF), a particle physics process known as Timelike Compton Scattering (TCS), given by the reaction $\gamma p \rightarrow pe^{+}e^{-}$, can be used to help potentially explain this discrepancy. With an eventual goal of providing a comparison of the experimental GlueX TCS data to Generalized Parton Distribution (GPD) models, initial research focused on isolating a pure TCS signal from a larger data set containing primarily the background reaction $\gamma p \rightarrow p\pi^{+}\pi^{-}$. After identifying and placing range restrictions upon experimental variables which are sensitive to the differences between $e^{\pm}$ and $\pi^{\pm}$ data, next steps included identifying the scattering plane angles of the electrons and positrons; significant variables in the cross section ratio present in GPDs. Our resulting plot of the ϕ plane vs detected $e^{+}e^{-}$ events indicated that the application of the restrictions that I selected and implemented to a larger data set will make it possible to more conclusively determine the presence and receptivity of TCS to GPD parameters.

Chapter 1: Introduction

1.1 Experiment Rationale

A proton's structure can be examined by accelerating particles to high energies, directing them to interact with a target comprised of protons, and analyzing how they or other produced particles have scattered. Particle accelerators use magnetic fields to direct the motion of the charged incident particles of the reaction in order to increase their velocity, which in turn increases their energy. The amount of kinetic energy lost by the incoming particles as a result of interacting with the target is balanced with the output scattered particle or particle production energy due to the conservation of energy. When high energy incoming particles from a particle accelerator interact with the fundamental particle components within the target particles, information about those fundamental particles – or the structure of the target particle – can be conceived from the resulting scattering energies, momenta, angles, and further reactions within a detector.

The Thomas Jefferson National Accelerator Laboratory (Jefferson Lab) houses one of the highest energy particle accelerators in the country, the Continuous Electron Beam Accelerator Facility (CEBAF) [1]. This makes its use an ideal source of knowledge for studying proton structure, since a higher energy and intensity beam is capable of yielding greater experimental precision for particle measurements.

Timelike Compton Scattering (TCS) is a useful reaction to examine in order to better understand proton structure because the electron (e^-) and positron (e^+) which it produces have a large

enough mass to become 'sensitive' to Generalized Parton Distribution (GPD) models, which many other reactions are unable to do. GPDs, which are probability distribution functions of the transverse position and longitudinal momentum of the quarks within a proton, have been proven capable of describing experimental parameters of the particle physics reaction known as Deeply Virtual Compton Scattering (DVCS) [2] — which is the inverse reaction of TCS and the reaction for which GPDs are the most easily accessible. GPDs have additionally been constrained by some observations of the DVCS process, thus further detailing a protons' structure. Figure 1.1 depicts Feynman diagrams of the TCS and DVCS processes, drawing attention to their similarities.

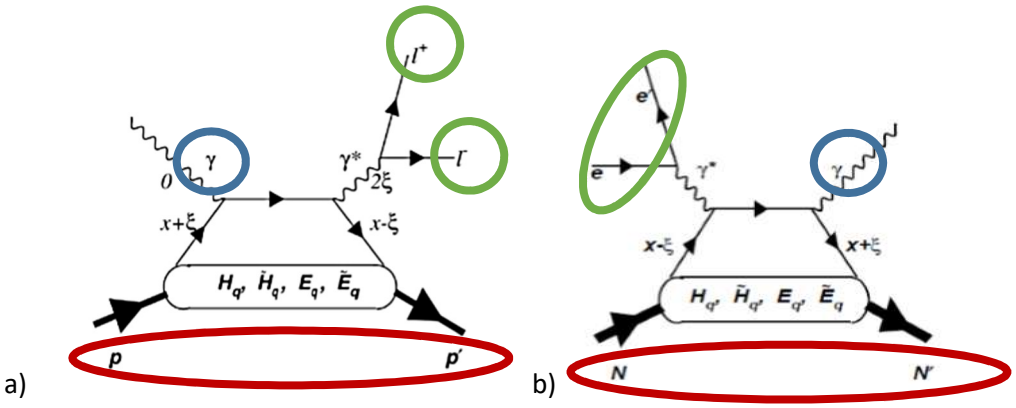

Figure 1.1: Diagrams of the TCS (a) and DVCS (b) reactions. The incident photon beam γ and produced particles e^+, e^- (written as l^+, l^- for lepton) in TCS correspond to the electron and output photon γ in the DVCS reaction, respectively. Corresponding parts of the reactions are circled in matching colors in the diagram. Parameters such as $x \pm \xi$ represent small momentum changes, and GPDs H_q, $\widetilde{H}_q$, E_q, and $\tilde{E}_q$ are shown to be extractable for either reaction.

A reaction's sensitivity to GPD factorizations results from taking measurements with a 'high scale' probe, provided in the case of TCS by the square of the e^+e^- four-momentum sum, $(M_{e^+e^-})^2$, which is also represented for TCS with the variable Q'^2. A large Q'^2 value allows observations to be made over very small distance scales, which is highly beneficial for

examining a proton's interior. A ratio which is highly useful for model-to-experiment comparisons, $R = \frac{2\int_0^{2\pi} d\phi \ \cos\phi \frac{dS}{dQ'^2 dt\, d\phi}}{\int_0^{2\pi} \frac{dS}{dQ'^2 dt\, d\phi}}$, provides the total weighted cross section for TCS, or the angle-dependent likelihood of the process occurring. The ratio R can be calculated from the scattering angles of the TCS experimental data and predicted theoretically from GPD models, which allows for their comparison [3]. Examining TCS in the context of GPDs provides a unique opportunity to test the universality of GPD models, or their ability to fit experimental data from not only DVCS but many processes. Since DVCS and TCS share several features, such as particle scattering amplitudes and their sensitivity to GPDs, TCS a good reaction with which to begin these comparisons.

TCS has been previously studied in another apparatus at Jefferson Lab besides the GlueX detector, the CLAS detector in Experimental Hall B, which proved the capability of making comparisons between the TCS reaction and GPDs [4]. However, it was also difficult to compare the CLAS detector's data with GPD models due to the limited mass range of its observations. Examining the TCS reaction using the GlueX Detector of Experimental Hall D provides a larger $M_{e^+e^-}$ range and also allows for the utilization of a higher energy electron beam, which was part of the recently completed 12 GeV Jefferson Lab upgrade. The upgrade allows GlueX to provide greater experimental precision than the previous study, which operated at approximately half the GlueX beam energy. Several different GPD observables can also be studied from GlueX data due to the photon beam's linear polarization, another feature which is unique to the detector. Linear polarization provides the capability of calculating additional variations of cross section ratios for the interference of TCS and non-TCS reaction scattering parameters, allowing the data to be sensitive to different combinations of GPDs [5].

1.2 Theory

Protons, once thought to be 'fundamental' particles comprised of no smaller units, are now understood to be baryons, or particles which are made up of 3 valence quarks held together by force carrier particles known as gluons. While non-valence quarks are temporary particles which are emitted and absorbed within a proton, valence quarks are the source of a proton's quantum numbers – the values which determine the properties of a quantum particle, such as its electric charge [6]. Of a proton's three valence quarks, there are two 'up' quarks and one 'down' quark—'flavors' which describe characteristics of quarks such as their mass or stability. A significant feature of quarks and other particles governed by quantum mechanics is spin, the intrinsic angular momentum of a particle, which when added to orbital angular momentum is equal to the particle's total angular momentum [7].

Until an experiment by the European Muon Collaboration in the late 1980s, this was believed to be the comprehensive explanation for proton structure, since a proton's spin (+ ½) equals the sum of the spins of its three quarks, which by including both the spin magnitude and 'projection' quantum number— or direction – would be +½ for each up quark, and -½ for the down quark. However, the sum of the spin contributions of each quark to the proton's spin is now understood to account for only approximately 25% of the total proton spin. Figure 1.2 depicts diagrams of how the proton structure was believed to look shortly before the EMC experiment in the 1980s and presently.

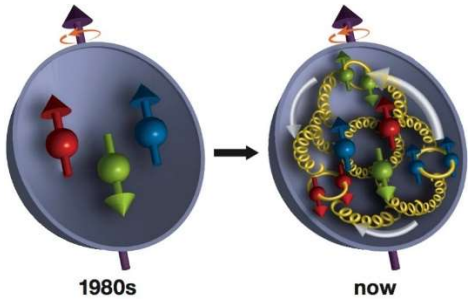

Figure 1.2: Diagrams of proton structure reflecting the available knowledge from the 1980s (with 3 valence electrons and their spin directions represented by the balls with up or downward arrows), and in the 2010s (with added orbital angular momentum represented by white arrows, gluons as the yellow springs, and the added sea quarks)

The lack of explanation for this spin difference is often known as the "proton spin crisis" [8]. Gluons—strong force particles which bind a proton's quarks together—and the orbital angular momentum of quarks within the proton are two potential sources of the remaining spin. As such, the distribution of gluons and quarks that make up a proton is a topic studied by many experimental collaborations and is the focus of this project.

1.3 Physics of TCS and other GlueX reactions

Timelike Compton Scattering occurs when a photon interacts with a proton, causing the emission and scattering of an electron and a positron (the latter of which is the antiparticle of the electron, having opposite charge but otherwise identical properties to an electron). The scattering of the electron and positron is symmetric, meaning that their scattering angles into the GlueX apparatus for each collision event should be identical except for their charges—something which is somewhat rare for the products of a particle physics reaction.

The types of particles which may be produced in the GlueX Detector are limited due to a conservation of charge, mass, and baryon number, which are limited by the incoming photon's energy. One reaction which was computationally difficult to separate from the TCS reaction in

our dataset was the production of another pair of positively and negatively charged particles known as pions (π^+, π^-), or pi mesons, which have similar masses to the $e^+e^-$of TCS. The pion data is also difficult to automatically separate from TCS data due to the near indistinguishable difference between the lengths of time taken for e^+e^- and charged pions to travel the length of the GlueX apparatus because of their relativistic nature at high speeds in the detector. Similarly, two other processes which result in the production of an electron and positron were significant to the data set utilized for this project, though they differ from TCS due to the intermediate steps of their reactions. In one such reaction, a J/ψ meson – a type of particle comprised of a quark-antiquark pair – is produced before decaying into an electron and positron. A process known as Bethe-Heitler (B-H) similarly produces an electron and positron, though its interaction involving a virtual photon rather than direct interaction of the incoming real photon with the quarks in the proton prevents it from providing a comparison to GPD models [9]. While these two reactions produce the same product which we sought to examine, they cannot be used to study GPDs, which require directly-produced electrons and positrons. Diagrams of the processes besides TCS which were produced in the GlueX apparatus and part of the data set that I examined are depicted in Figure 1.3.

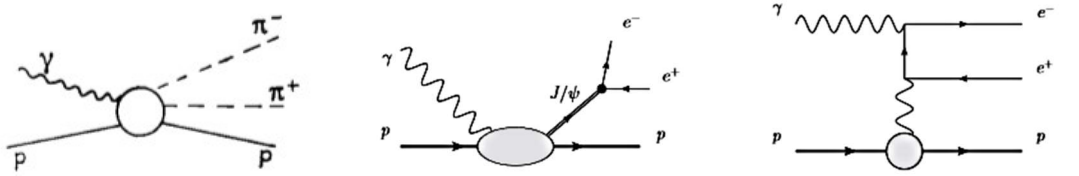

1) $\gamma p \rightarrow \pi^+\pi^-$ 2) $\gamma p \rightarrow [meson]p$, $[meson] \rightarrow e^+e^-$ 3) Bethe Heitler process

Figure 1.3: The three reactions produced along with TCS during the experiment, two of which produce the same end products as TCS. For the middle reaction, different mesons may be produced and decay into e^+e^-

Chapter 2: Experimental Setup

2.1 Experimental Apparatus

The GlueX apparatus, depicted in Figure 2.1a, is located in Jefferson Lab's Experimental Hall D, one of four offshoots from the CEBAF main accelerator loop and a site where the studied particle interactions and production occur. Hall D is the most recently constructed experimental hall at Jefferson Lab, completed in 2017 as part of the facility's 12 GeV Upgrade, which additionally increased the accelerator's electron beam energy from 6 to 12 GeV. While by comparison, 12 giga-electron volts (12 GeV) of energy amounts to 1.9×10^{-9} Joules, or only 4.6×10^{-13} nutritional calories, it is a very large value for particles on a microscopic scale, allowing electrons in the CEBAF to reach relativistic speeds and produce other particles in their interactions. In the GlueX experiment, high energy electrons directed into Hall D from CEBAF are passed through bremsstrahlung radiators, which are designed to slow the electrons down due to the presence of charges in a thin diamond lattice. Due to the conservation of energy, the energy lost due to the electrons' decreasing kinetic energy is converted to produce a photon (γ), which is a reactant for TCS and the other GlueX reactions [11]. This resulting photon beam is then directed with a dipole magnet through an array of scintillators which provide the photons' energies by detecting the amounts of light they emit. Passage through a collimator and several polarizers then linearly polarize the photon beam [12] which ensures that its electric field direction remains constant, a useful characteristic for GlueX measurements for the reasons described in section 1.1.

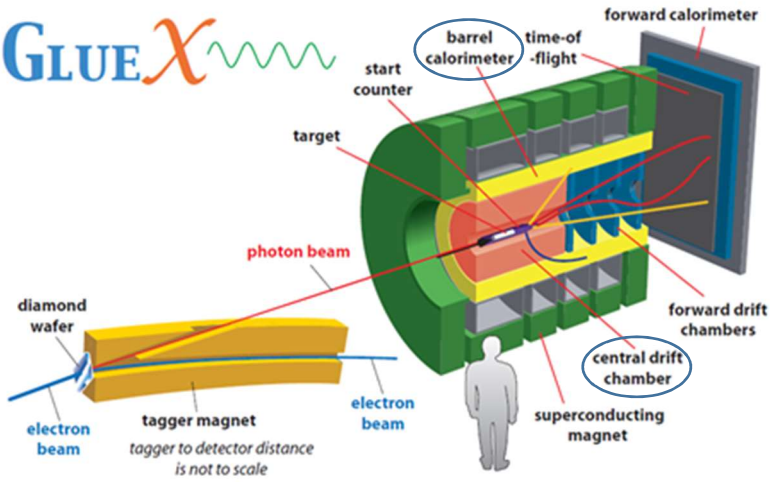

Figure 2.1a: A diagram of the GlueX detector layout. This project primarily utilized data gathered from the detectors in the barrel calorimeter and central drift chamber, the names of which are circled. The apparatus is explained in greater detail in the rest of section 1.3

The polarized photons then travel into the GlueX detector, where they strike a 30 cm long liquid hydrogen target and produce the reaction, resulting in scattered particles such as an electron and positron. Over the course of a data recording run, many instants of data leading up to and following this interaction are collected, providing information about the produced, incoming, or target particles in what are known as events.

Following the photon's interaction with the target, the scattered particles pass through a cylindrical instrument known as the Central Drift Chamber (CDC), which tracks their position over time and loss of energy dE/dx, and is useful to identifying the types of particles which were produced [13]. The CDC is surrounded by the Barrel Calorimeter (BCAL), which contains 4 layers of small modules which absorb energy when struck by particles [14]. The number of consecutive modules which a particle deposits energy into also aided in particle identification, proving particularly useful for separating the electrons and positrons from the charged pions, a process described further in Chapter 3.

The energy dissipated in BCAL modules is categorized by spatial orientation using the angular variables ϕ, θ, and r. Phi (ϕ), also known as the 'transverse' angle, which is abbreviated in the data variable names as 'trans', describes the position around the detector at which particles strike the BCAL, much like angles created by the hands of a clock, where the clock face is the view looking into the cylindrical BCAL. Theta (θ) describes the angle forward into the BCAL when viewing the detector in the direction following the entering photons, and completing the trio of cylindrical angles is rho (abbreviated simply as 'r'), the depth radially outward in the BCAL, which is also known as 'longitudinal', or 'long'.

Sigma values, $\sigma_x = \sqrt{\frac{\sum(x-\bar{x})^2}{n}}$, of each of these variables refer to scattering angle distribution widths, or the number of the side by side modules which are filled in each direction by the particle shower. For the calculation of sigma values, 'x' represents each BCAL module into which a fraction of energy from one reaction's outgoing particles has been released, where each module is identified by its angle θ, ϕ, or 'r'. $\bar{x}$ is the mean position of the energy-filled modules and 'n' is the number of modules filled. Figure 1.3b illustrates the orientation of the angles and widths within the BCAL.

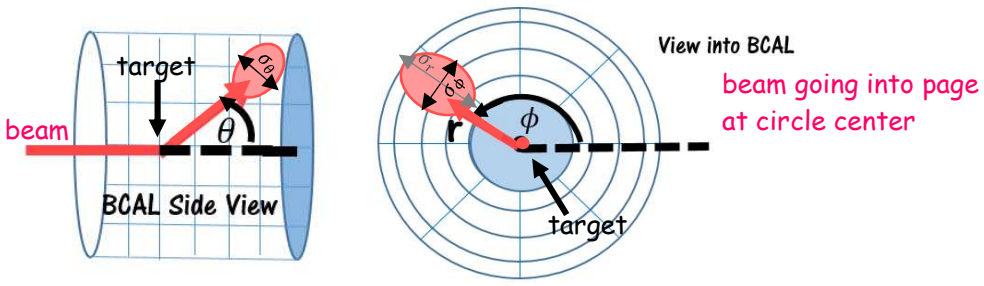

Figure 2.1b: GlueX Detector particle scattering angles θ, ϕ, and r

A ratio known as the Preshower/Shower Energy ratio ($E_{\mathrm{Preshower/Shower}}$) makes use of the depth measurements, comparing the amount of energy dissipated in the first layer of modules to the outer three layers. The BCAL angles and the standard deviation, sigma, of the energy dissipated for each are the primary variables described in the histograms of GlueX data, and are described further in Section 3.1.

At the end of the GlueX detector is the forward calorimeter (FCAL), which absorbs the energy of particles which scatter at smaller angles than those that impact the BCAL interior. The entire GlueX detector is surrounded by a large solenoid magnet producing a constant field of 2T, which contributes to the measurement of particles' momenta [14].

2.2 Data Set Organization

The data set for this project consists of a subset of the approximate 1 petabyte (one million GB) of GlueX data collected in Spring 2017. The events which I examined were initially selected using parameters such as the number and charges of particles they produced, which resulted a data set comprised of the four remaining reactions described in section 1.3. I examined approximately 310 runs, containing approximately an initial 15 billion events.

My initial data set additionally contained several dozen histograms contrasting the different GlueX variables for which scattered particles were observed, such as the BCAL scattering angles and energy shower distributions. The C++ code for making these histograms is included in the GlueX DSelector class for TCS data, and this DSelector script was the source in which further edits to adjust variable cuts for isolating TCS data were applied.

Histograms for each pair of GlueX variables were created separately for electron and positron candidates. These candidates each also contained the charged pion data of their corresponding

charge due to the inability to separate the reaction products using only the initially applied data set restrictions.

The histograms were further classified by an initial cut which separated data within the mass range of 3.07 GeV/c^2 to 3.12 GeV/c^2 and that from 2.0 GeV/c^2 to 3.0 GeV/c^2. The former mass range contains the mass of the J/ψ meson, 3.096916 GeV/c^2, which due to its decay into the lepton pair contained a reliable source of primarily e^+e^- data. This data is referred to with the histogram title suffix 'J/ψ' and was useful for comparing the collected e^+e^- data with pure e^+e^- simulated data. Such comparisons could determine whether e^+e^- production was occurring and successfully detected within the GlueX apparatus in the expected manner—details which would be difficult to see in combined e^+e^- and $\pi^+\pi^-$ histograms within other mass ranges due to the latter products' dominating production frequency. Charged pions were produced in the GlueX apparatus much more frequently than electrons and positrons due to the experimental 'probe' for our experiment being a photon, which tends to produce hadronic interactions – involving mesons such as the charged pions, rather than leptons. As such, the data in the lower mass range restriction is labelled as 'Background' and contains predominately charged pions. The background mass range was selected in order to prevent meson resonances, or excited mesons such as the excited rho meson (ρ') at ~ 1.5 GeV/c^2, from interfering with the data [15].

Another useful plot provided in the dataset was the mass histogram, which depicts the masses of the pairs of detected collision products, such as e^+e^-. A mass histogram contains a continuum of masses rather than well-defined peaks at each particle's mass because it is dependent on invariant mass, the square of the sum of the four-momenta of the particles. As a result, a particle moving with greater momentum in the GlueX detector will have a larger

detected mass than the same type of particle with smaller momentum. Bethe-Heitler, TCS, and some $\pi^+\pi^-$ particles are produced with a notably wider range of masses because they do not decay from mesons, which would limit their possible masses to around that of the meson as is the case with the particles that decay from J/ψ or ρ. Our main analysis included data for particles with masses spanning the entire Background region due to this variation in the masses of e^+e^- produced by TCS. Comparing mass histograms before and after additional GlueX variable restrictions were placed allowed us to determine of whether charged pion data had been successfully removed, as will be described further in section 3.2.

A mass histogram depicting the J/ψ and Background mass cut ranges and the mass regions of the particle pairs produced in the GlueX experiment is presented in Figure 2.2.

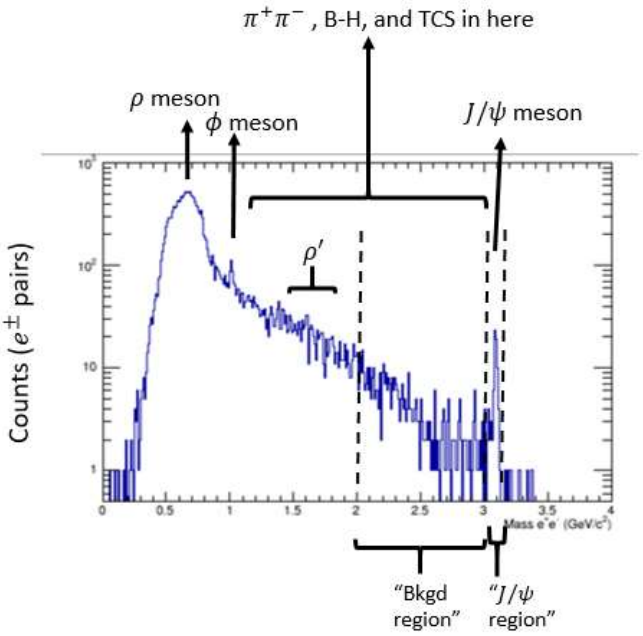

Figure 2.2: A mass histogram illustrating the invariant masses of particle pairs produced in the GlueX experiment, including J/ψ = 3.09 GeV/c^2, ρ = 0.77 GeV/c^2, and ρ' = 1.5 GeV/c^2. Many pions decay from the ρ meson, while e^+e^-decay from the J/ψ meson. Mass histograms were useful to identifying whether pion data was successfully removed from the data set.

Chapter 3: Event Selection and Methods

3.1 Removing $\pi^+\pi^-$ Background

Removal of the charged pion data in our data set was the first step necessary for isolating TCS due to the pion reaction's much larger set of events compared to the other three reactions, which would drown out their data, preventing the more finely-detailed analyses required for the latter reactions' separations from initially being made. The differing product of charged pions compared with the e^+e^- of TCS and the other two reactions was the basis from which we made the $\pi^+\pi^-$ subtraction.

With access to the initial histogram data and the particle physics programming language ROOT in the William and Mary High Performance Computing cluster, I first combined the GlueX data for the all of the events collected in the run files. This was necessary due to the low and often single digit number of events contained in each run for e^+e^-, with an even lower expected rate for the rare TCS process. As such, the combined data provided greater statistical confidence in our analysis while allowing correlations of the reaction data to different GlueX parameters to be more easily recognized.

The process of isolating TCS data was carried out by comparing data in the Background and J/ψ histograms to a set of data simulated using the Monte Carlo method, depicting the scattering parameters of purely e^+e^- reactions. The Monte Carlo simulation used known characteristics of the electrons and positrons – such as their masses, charges, and expected energy and momentum values– and generated possible results for how e^+e^- would scatter and

produce showers by repeatedly pulling random samples of a dataset calculated from that prior information and determining which production parameters would be most probable.

By identifying shared patterns between the Background and J/ψ histograms, the plot regions of the J/ψ histogram which were dominated by charged pions could be visually identified—since the majority of the former's data was pions, whereas patterns shared by the simulation and J/ψ histograms marked regions of predominately the e^+e^- products. As such, the J/ψ plots served as an ideal canvas from which to visually deduce the most useful variable cuts for $\pi^+\pi^-$ subtraction. Figure 3.1a contains a graphic of the Background, J/ψ, and Simulated 2-D histograms generated to examine e^+e^- and $\pi^+\pi^-$ sensitivity to a pair of GlueX variables.

A second and less qualitative method for identifying which histogram regions contained electrons and positrons and which contained charged pions involved examining the plots for known features of electrons and positrons which differed from those of pions. These parameters were determined from an understanding of the underlying physics affecting each type of particle within the GlueX detector. One GlueX variable that we examined using this method of particle identification was the ratio of the energy to the momentum of the particles, E/p, which was calculated from BCAL energy measurements and CDC charged particle tracking, which could be used to calculate momentum due to its recording of the position and energy of the particles over time [13].

An E/p ratio of approximately 1 is expected for the e^+e^-data, whereas it is smaller for pions. The ratio is larger for e^+e^- because electrons and positrons are more reactive to the layers of the BCAL than $\pi^+\pi^-$ due to the types of interaction required to produce a particle shower for each. The e^+e^- react electromagnetically, slowing and producing photons in the BCAL due to the electric fields of the BCAL modules' lead atoms. As is the case for either reaction, photon

production allows the BCAL apparatus' light-collecting scintillators to determine the particles' energy loss per module, as the detectors correlate this with the number of emitted photons which have been detected as particles pass through their modules.

On the other hand, charged pions react hadronically—meaning that they do not produce photons unless they directly interact with the nuclei of the lead, a much less frequent occurrence [16]. As such, e^+e^- are more likely to deposit all of their energy into the BCAL detector, while $\pi^+\pi^-$ react to impacting the BCAL lead layers less often, consequently depositing a smaller fraction of their energy while passing through them, which results in their having a smaller numerator of E/p and a smaller ratio value overall. This is also apparent in Figure 3.1a, where the e^+e^- region forms a horizontal band at the value E/p = 1 in the J/ψ and simulation histograms, whereas it is smaller for $\pi^+\pi^-$.

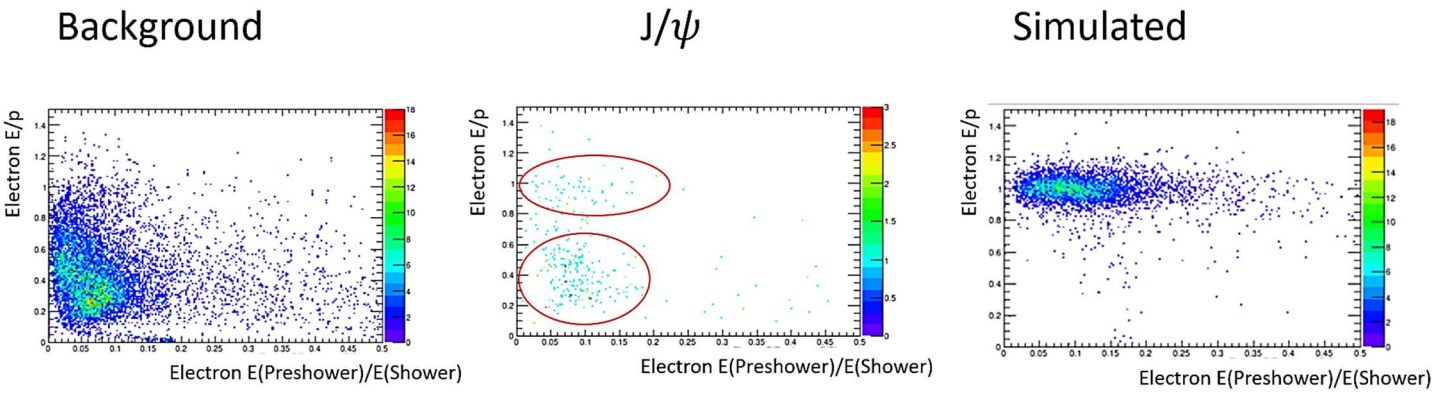

Figure 3.1a: Histograms of GlueX experimental data (Background, J/ψ) and e^- Monte Carlo simulated data used to visually identify differences between the electron and charged pion scattering behavior in the BCAL detector. The e^- and π^- regions present in the J/ψ plot can be deduced from the dense particle regions in the Background and Monte Carlo simulation plots. The histograms set the E/p ratio against the Preshower/Shower Energy ratio, parameters which can also aid with particle identification due to an understanding of the particles' properties such as reactivity to the BCAL modules. The positively charged counterparts of the depicted particles react identically, and would later be included.

Expectations of the e^+e^- and $\pi^+\pi^-$ values of the $E_{\text{Preshower/Shower}}$ ratio can be examined similarly. Once again due to their greater reactivity to the BCAL material, e^+e^- deposit a larger fraction of their energy within the innermost circle of BCAL modules, providing a greater Preshower energy and larger ratio value overall. Because $\pi^+\pi^-$ often do not react until further into the detector, they have a smaller Preshower energy value compared with the amounts of energy they deposit into the outer BCAL layers that provide their Shower energy, causing them to have a smaller $E_{\text{Preshower/Shower}}$ ratio. This difference between e^+e^- and $\pi^+\pi^-$ is visible in Figure 3.1a, where the majority of the particles detected in the Background histogram of primarily pions have a $E_{\text{Preshower/Shower}}$ ratio below 0.15, whereas the densest particle region extends past a ratio value of 0.20 for the e^+e^- simulation.

The BCAL shower widths are a final source of comparison between the particle products which we aimed to separate, and were distinguishable due to a narrower expected width for e^+e^- compared to $\pi^+\pi^-$. This is due to hadronic interactions depositing a larger fraction of their energy when they occur, providing enough energy for more secondary particles to form and scatter [16], which causes multiple additional photons to be produced over a shorter distance through the BCAL. Figure 3.1b depicts an experiment diagram from another accelerator apparatus – the European Large Hadron Collider ATLAS experiment at CERN – which demonstrates differences in scattering angle widths and initial energy deposits as a source of particle identification.

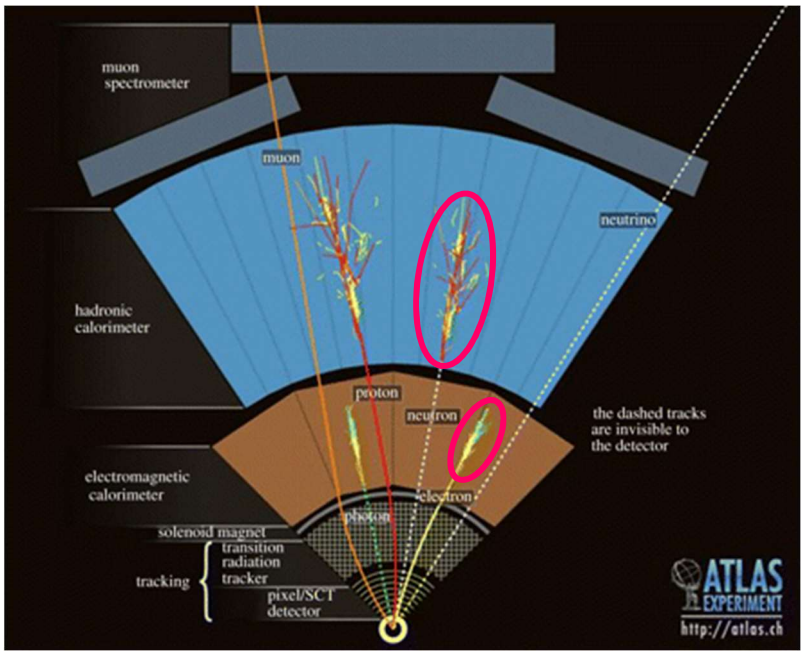

Figure 3.1b: Particle identifications based on scattering and absorption parameters within calorimeters in the ATLAS experiment at the Large Hadron Collider (LHC), the world's largest particle accelerator. The electron scattering (the lower right circle) scatters with a narrower distribution, begins its shower earlier than, and has energy deposited over a shorter distance than the proton and neutron, which interact hadronically much as pions would.

In order to more easily identify histogram patterns for J/ψ or Background data, it was useful to first combine the electron and positron data and increase the bin sizes of the histograms. Combining the electron and positron data was possible due to their scattering symmetry, as charge polarity has little effect on their motion in the GlueX apparatus. As such, combining the two increased the size of the data set, strengthening and darkening density markings in the two dimensional histograms to make regions of charged pions or electrons and positrons more apparent.

Similarly, increasing bin sizes increased the density and thus visibility of plot regions with both particle types while having a lesser effect on outlier data. Re-binning the e^+e^- simulation plots by different amounts helped to find a balance between limiting the plots' empty space and preventing a reduction of the pixel resolution to magnitudes at which the pion and TCS data

smeared together. The re-binning factor which suited the histograms best in this manner divided the initial number of bins by 4, and this was applied to all histograms. The difference between combined and re-binned data from that in original formatted histograms is depicted in Figure 3.1c.

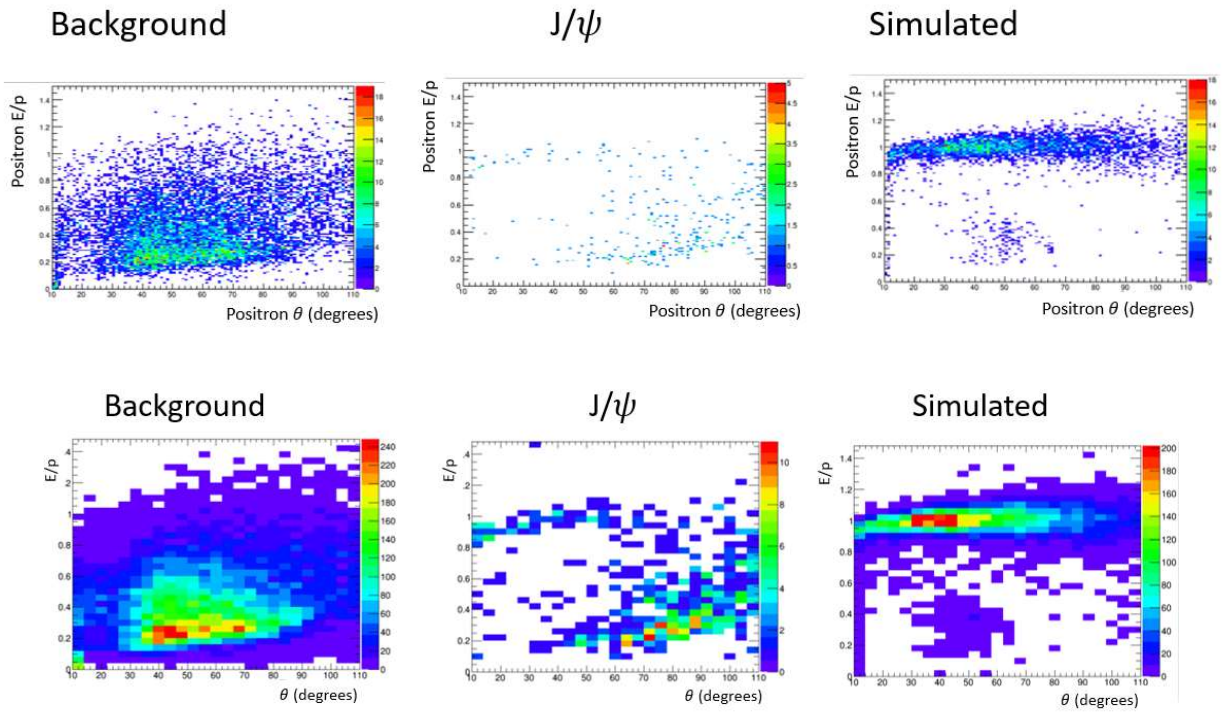

Figure 3.1c: This series of plots, depicting the BCAL E/p ratio vs the BCAL angle θ, demonstrates the difference in clarity of TCS and charged pion regions within histograms after combining electron and positron data and increasing the bin sizes by a factor of 4, which has been implemented in the bottom row.

An examination of the preselected DSelector cuts for the GlueX variables provided a good starting point from which to decide what further limits should be placed on the data. Besides the J/ψ mass range cuts which divided the data, several additional cuts were coded into the DSelector but were not yet used to separate histograms and isolate e^+e^-. The first of these was the CDC cut, which relayed energy loss dE/dx within the GlueX detector and removed data below its given function curve, $\mathrm{dE/dx} = 2.2 - 0.00015 * \theta^2$. The second pion subtraction

cut was the Shower shape cut, which removed data from detected events for which energy was deposited into BCAL modules with a transverse width greater than $\sigma_\phi = 0.018 - 0.035 * (E_{Preshower/Shower} - 0.5)^2$. The format of both variable restrictions within the DSelector served as a useful guideline for constructing the cuts which we later selected and employed, while additionally providing a demonstration of the effects of different applied cuts on changes and prominent regions of change to the event counts in a mass histogram of the data set. Figure 3.1d contains this mass histogram depicting the number of detected particle events versus the combined mass of each pair of electron and positron candidates before and after the CDC and Shower shape cuts have been applied. As is expected, both cuts reduced the detected counts within the 2 – 3 GeV/c^2 mass range, which we could identify as a subtraction of pion background due to the number of counts in the J/ψ mass range remaining nearly constant—as this would have decreased more significantly if we had unintentionally removed primarily e^+e^- rather than $\pi^+\pi^-$ data.

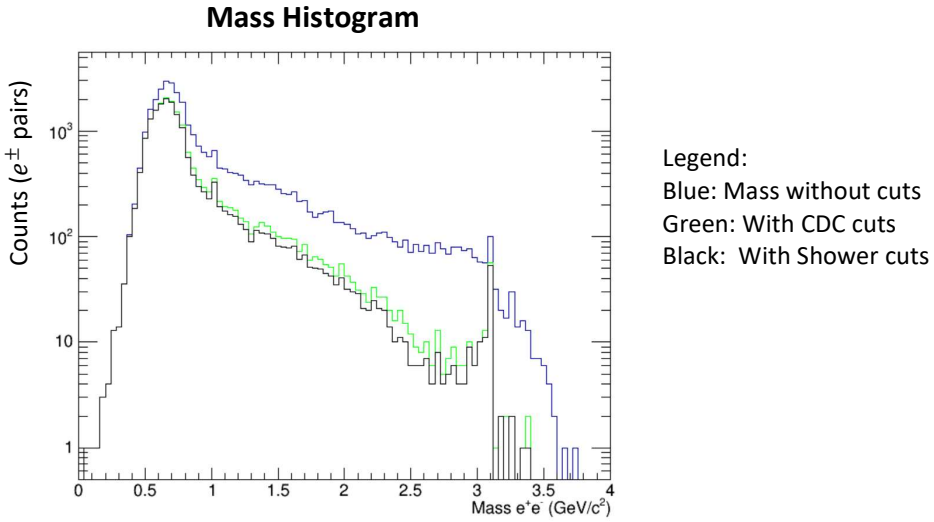

Figure 3.1d: This histogram depicts the sum of the masses of the electron and positron candidates as a function of the number of candidate pairs. The blue, black, and green curves indicate changes within the data set due to the removal of data as a result of successively applying the CDC and Shower cuts. It is apparent that the addition of CDC and Shower cuts successfully removes pion data since the J/ψ mass region located at ~ 3.09 GeV/c^2 becomes more distinct compared to the background region data as a result, indicating that e^+e^- make up a larger fraction of the data. The log scale of the y-axis is used to make changes in the larger mass regions more clear.

The removal of the correct particle type when cuts were applied was also demonstrated by plotting the 2-D histograms of the two variables with which cut values were chosen. Plots utilizing this latter confirmation method will be depicted with each of the cuts we implemented in section 3.2. The cuts which we ultimately applied were also more restrictive than the CDC and Shower cuts, thus negating the necessity of applying the latter two to the data.

3.2 Employing Cuts

After a qualitative examination of the GlueX e^+e^- candidate histograms, we determined five restrictions to place on the GlueX variables which were most responsive to the differences between charged pion and e^+e^- data, allowing us to remove the maximum pion data. Each of the five restrictions was added to the DSelector script and was used to generate a new mass histogram plot and 2-D histograms of the Background mass range data for the plot which was used to determine the cut, for which the data subtraction would be most apparent in an expected range. A figure depicting the changes in the mass histogram over the five cuts is depicted in Figure 3.2a.

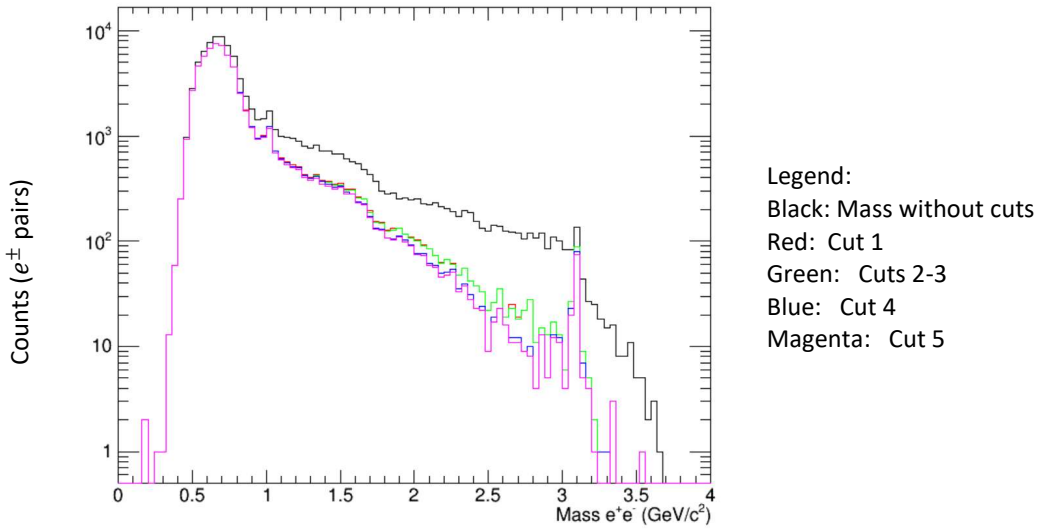

Figure 3.2a: A mass histogram of the five cuts we selected and placed on the data set to remove charged pion events. While the cuts were individually not successively more restrictive, they were implemented under the condition that the previous cut had already been applied, resulting in greater total pion reduction through each successive cut.

Examining the J/ψ plots, with e^+e^- events from 3.07 – 3.12 GeV/c^2, was no longer necessary after their use in determining the histogram variables to which restrictions for separating the e^+e^- and $\pi^+\pi^-$ would be best applied. This is due to our primary goal of isolating TCS, for which the produced electron positron pairs resided within the 2-3 GeV/c^2 mass range along with those produced by the B-H process. Therefore, once our variable restrictions were applied, it was possible to analyze e^+e^- which were potential TCS candidates since the pion background no longer impeded their visibility.

The first cut which we applied, $\sigma_\theta > 0.1951 * \left(E_{\text{Preshower/Shower}}\right)^{0.5} - 0.0195$, is a curved function similar to the CDC cut described in the section 3.1. The cut, labelled as 'ACCutsR1' in the DSelector code, removes the larger theta width angles at smaller $E_{\text{Preshower/Shower}}$ values, with the form ~ $\sqrt{x}$. While narrower shower widths and larger $E_{\text{Preshower/Shower}}$ values were expected of electron and positron data, the correlation of the two variables was made prominent in the 2-D histogram of both, demonstrating that the application of this restriction would be highly beneficial for removing charged pion data.

The fit for the function was determined by selecting plot points along the edge of the identified dense pion data region from the Background plot of the σ_θ vs $E_{\text{Preshower/Shower}}$ histogram, plotting in Matlab, and applying a built-in fit function of different function forms until there was close visual alignment between the data points and the fit curve. Figure 3.2b depicts the implementation of this initial cut in the σ_θ vs $E_{\text{Preshower/Shower}}$ histogram, with the data set before and after its placement.

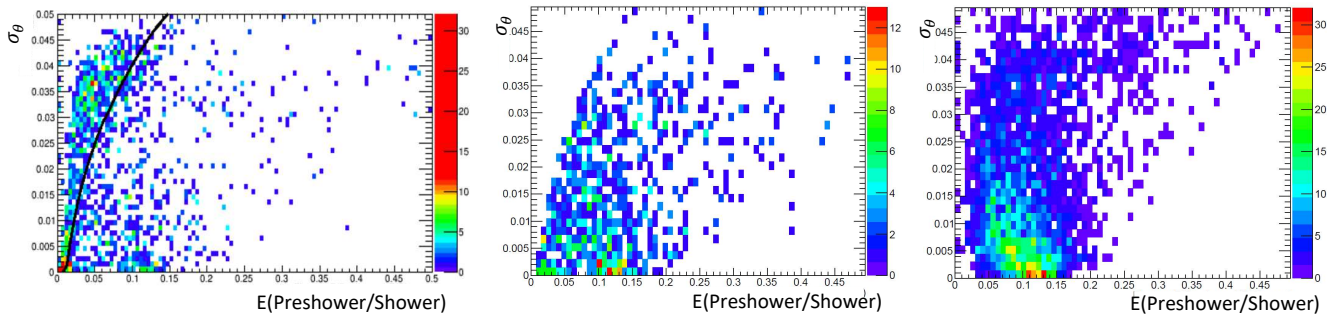

Figure 3.2b: Background histograms for Preshower/Shower energy ratio (x) vs σ_θ (y) before and after the first restriction was implemented, followed by the simulated e^+e^- data histogram. The middle plot demonstrates that the majority of the dense pion data has been removed, while the region of remaining data contains the densest e^+e^- region. The black curve in the Background plot indicates the cut function.

The second cut, removing $\mathrm{E}_{\mathrm{preshower/shower}} < 0.015$, supplemented the first cut by taking out the small data region at the base of the Cut 1 curve where a small notch in the fit function left a dense pion region. A second histogram which was useful in separating the e^+e^- and $\pi^+\pi^-$ data was the σ_ϕ vs σ_θ plot, for which the standard deviation of theta was notably larger for the pions, as is expected. As such, the third restriction was placed on the variable σ_θ, removing data where $\sigma_\theta > 0.025$. Figure 3.2c depicts the application of Cut 3.

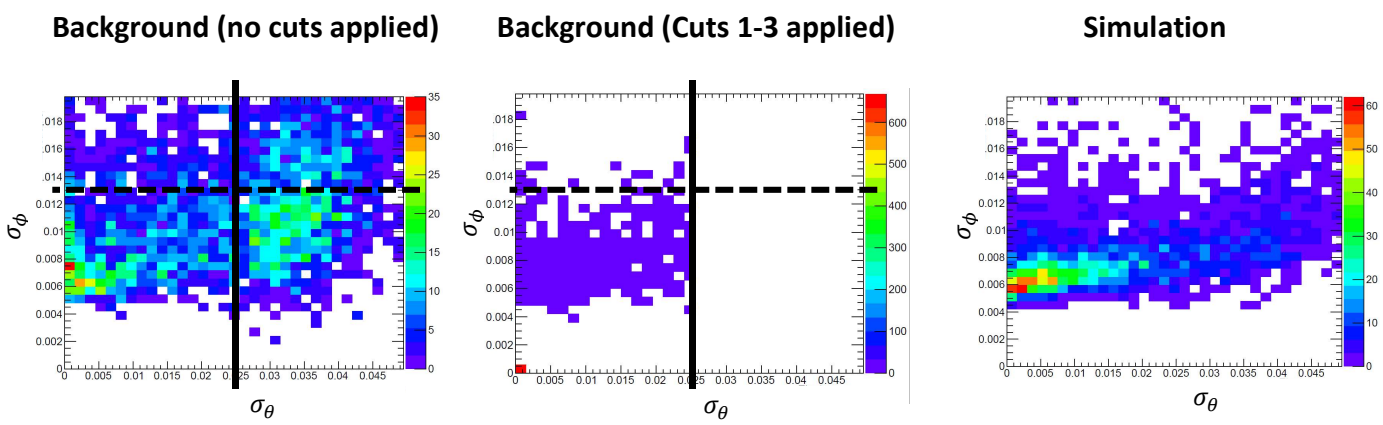

Figure 3.2c: Application of the third successive cut, on the σ_ϕ vs σ_θ histogram. Data to the right of the solid vertical line in the Background plots was removed, subtracting the dense pion region which was present in the right quadrants. The horizontal dotted line in the Background plots indicates where the fifth cut was applied and data greater than $\sigma_\phi = 0.013$ was removed.

Parameters for the fourth cut were determined using the E/p vs θ histogram. The E/p ratio created a prominent contrast between the of the pion and e^+e^- data regions in these histograms, with distinct horizontal bands separating the TCS and pion E/p values due to their differing E/p ratios. The restriction removed all electron data below 0.75. Histograms for before and after the cut was implemented are depicted in Figure 3.2d.

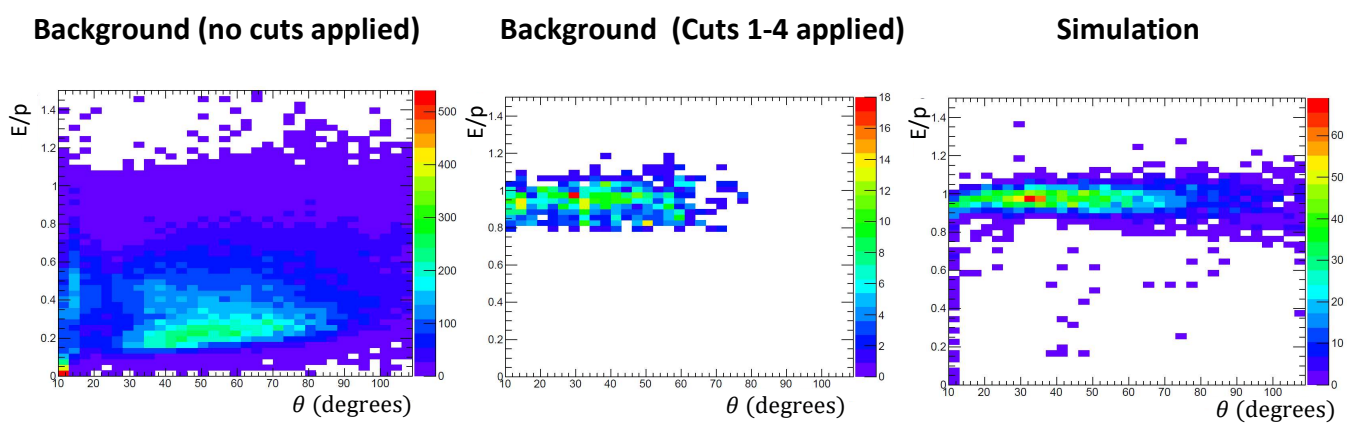

Figure 3.2d: Background histograms for θ vs the ratio of E/p before and after the fourth restriction was implemented, followed by the simulated e^+e^- data. At this later cut, the restricted background data (middle plot) much more closely resembles the simulated and thus primarily e^+e^- data than the comparison from Figure 3.2b.

A fifth and final cut, $\sigma_\phi > 0.013$, supplements the third cut and was selected by examining the σ_ϕ vs σ_θ histogram. Figure 3.2c depicts the this cut and the pion data which it removed.

The coded 'if statements' for which each of the five cuts was implemented additionally contained the stipulation that each event was only to be kept if both the electron and positron fulfilled the cut requirements, thus allowing for tighter restrictions. Excerpts of the DSelector script which contains the placement of these five cuts are located in Appendix A-1.

Chapter 4: Analysis and Results

4.1 Scattering Angle Analysis

Following the removal of pion data – as well as J/ψ data, which was done by limiting our mass range to 2 – 3 GeV/c^2 – we began analyses to remove B-H data, determine the presence of TCS in our data set, and calculate the cross sectional ratio R. The first step of this involved calculating the angles (ϕ, θ) of the electron and positron scattering planes. These differed from the angles which were depicted in the 2-D histograms because we now required that the electron and positron scattering be related to one another rather than travelling away at different angles following each individual reaction. The planes of e^+ and e^- scattering, known as the decay planes, were calculated with respect to the incoming photon plane, or production plane, as is depicted in Figure 4.1. The scattering plane angles were necessary to calculate due to the dependency of differences between the TCS and B-H processes, as well as the cross section ratio R— and therefore GPD parameters – on their values.

In order to calculate the plane angles, we needed to transform the coordinate system of the reaction into the resting reference frame of the produced e^+e^- pair such that they scattered symmetrically, with a 180 degree angle between them. This was done by applying two Lorentz boosts, mathematical calculations which multiply the x, y, z, and time coordinates of a reference frame by a matrix of relativity equations in order to shift the system into a new reference frame.

The first Lorentz boost was applied to the reaction's lab frame – the coordinate system of the histograms and the apparent directions of motion and scattering according to an outside

observer of the experiment. The boost transformed the incoming photon beam (γ) into a new reference frame within which the γ and p approached each other directly such that in the moment of their interaction their momentum values would be equivalent in magnitude and cancel, making the reaction effectively at rest. This allowed the resulting scattering of the e^+e^- to be independent of the experimental production and measurement methods, such as variations in the kinetic energy of the arriving photon.

As such, with the transition into this 'γp frame' scattering of the e^+e^- became dependent solely on the required energy of their production and the proton's structural characteristics, allowing for consistent measurements relating to the particle properties, which we desired for examining the structure of the proton. The first Lorentz boost is depicted in the lefthand diagram of Figure 4.1.

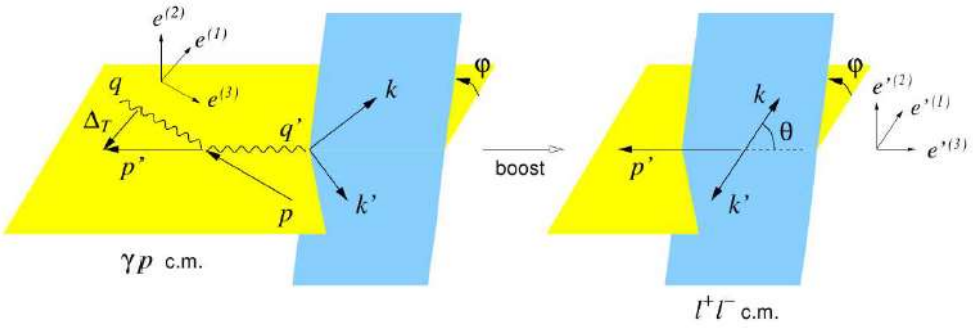

Figure 4.1: A depiction of the Lorentz boost from the frame of reference of the photon and proton to that of the electron and positron. The k and k' represent the e^+ and e^- in the diagrams, the yellow plane is the production plane, and the blue plane is the decay plane. The e and e' coordinate directions indicate that the reference frame was shifted between the left and righthand diagrams. The initial boost to place the photon beam into the γp rest frame is depicted in the left hand diagram, as is demonstrated by the arrow indicating the motion of the proton p towards the photon γ, which was in fact part of a stationary target. The second boost is depicted in the righthand diagram.

A second Lorentz boost was then applied to the γp frame, transforming it into the rest frame of the e^+e^- as is depicted in the right hand diagram of Figure 4.1. Several more excerpts of the

DSeletor code, containing the application of these two Lorentz boosts, are included in Appendix A-2.

4.2 θ range restrictions

In order to ensure that the e^+e^- scattering plane angles were correctly orientated and that the final reference frame had been calculated correctly, we then created a histogram of the projection $cos(\theta)$ onto the decay plane as a function of the plane angle ϕ. The $cos(\theta)$ histogram was useful due our expectation that in the final reference frame of the boosts the scattering of e^+ and e^- relate symmetrically, which would be clearly indicated by symmetry about the angle $\phi = 0$ in our histograms following an accurate transformation. Figure 4.2a contains the $cos(\theta)$ histograms which were created from our simulation and the remaining experimental data following all variable restrictions.

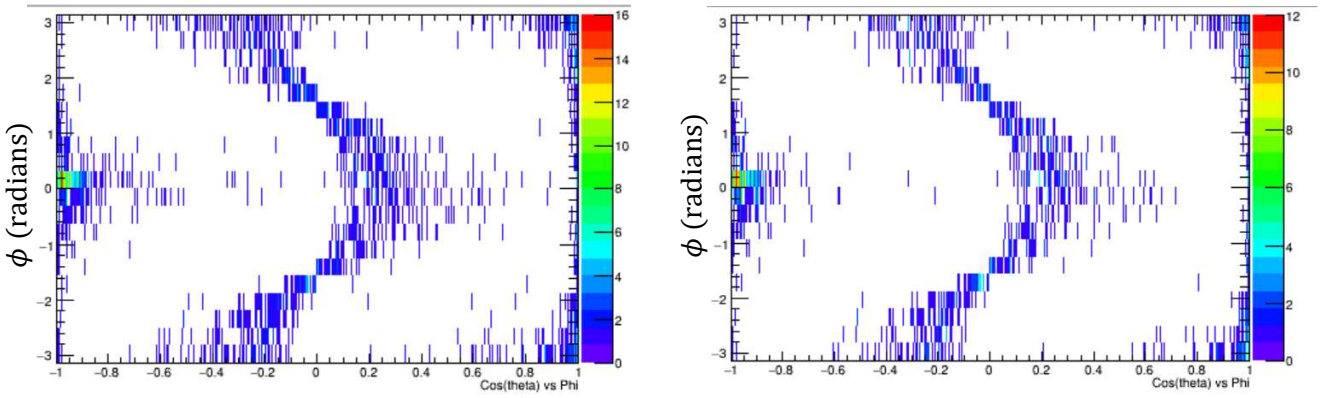

Figure 4.2a: The $cos(\theta)$ vs ϕ histogram for experimental (left) and simulation (right) data, which was used to validate that the Lorentz boosts were successful. The apparent horizontal symmetry to the left and right of the angle $\phi = 0$ correlates with the expected result.

Using the plane angles in the e^+e^- rest frame, some of the particles produced by the B-H process could then be removed due to the differing scattering angle dependencies of the B-H

and TCS processes. Electrons and positrons produced by the Bethe-Heitler process – while more common than e^+e^- produced by TCS at all angles – are expected to be most prominent outside of the θ angle range $[\frac{\pi}{4}, \frac{3\pi}{4}]$.

Figure 4.2b depicts the experimental data $\cos(\theta)$ histogram before and after the application of this θ restriction.

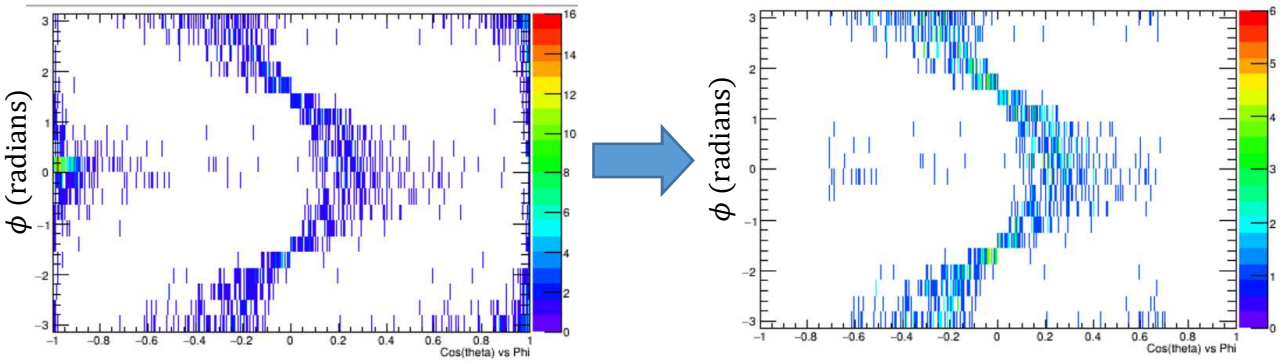

Figure 4.2b: $\cos(\theta)$ vs ϕ histograms before (left) and after (right) applying the range $\frac{\pi}{4} \leq \theta \leq \frac{3\pi}{4}$ to remove some of dominant B-H process e^+e^- production. The regions at (-1,0), (1, π), and (1,$-\pi$) in the first histogram are most prominently B-H events, and have been removed in the second histogram along with some events in the main curve, as is noted by its lower density.

4.3 ϕ histograms

Following the subtraction of this portion of the B-H events, another histogram— depicting the decay plane angle ϕ versus e^+e^- events – was helpful to the process of determining whether the remaining e^+e^- which were detected within the GlueX apparatus were produced as a result of the Bethe-Heitler or TCS reaction. The Bethe-Heitler process has a $cos(\phi)$ dependency, varying over the angles 0 to 2π, while TCS has a $cos(2\phi)$ dependence and therefore varies over half of the same range [3]. An examination of differences in the shape of the function formed by data in the ϕ histograms before and after the application of the θ range restriction could as such provide insights into whether TCS is present.

Plots of the theoretical and experimental ϕ vs events histograms before and after the θ range restriction was implemented are presented in Figure 4.3. The units of events on the y-axis of the histograms additionally provided an analogue to our intended cross section calculation, since the number of events which are detected is a combination of detector efficiency and the likelihood of production (cross section). Appendix A-3 contains excerpts of the DSelector code used to create both the cos θ and ϕ histograms.

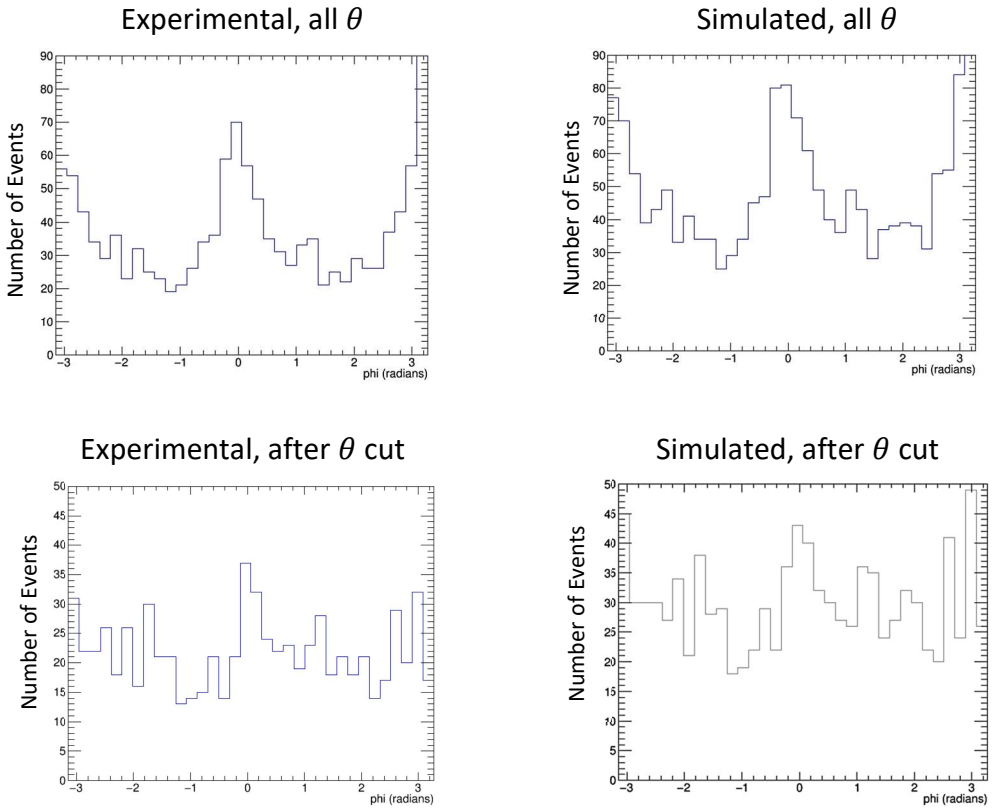

Figure 4.3: Histograms of the scattering plane angle ϕ with respect to the number of detected e^+e^- events, before (top row) and after (bottom row) the θ range limit $[\frac{\pi}{4}, \frac{3\pi}{4}]$ has been applied. The function shapes between the rows were compared to examine whether TCS is present and are useful for the calculation of R. The lack of symmetry in the number of events is a product of the adjusted coordinate system due to the Lorentz boosts.

As is apparent from the Figure 4.3 histograms, changes to the shape of the function before and after placing the θ range restriction are difficult to determine due to the low amount of statistics, though a slight periodic pattern does appear to be present in each as is expected. The

data was binned by a factor of 20 to reduce uncertainty. Despite this, the simulations indicate that given the size of our data set, the best possible charged pion subtraction would not provide a much more clearly defined cosine function for the data than was produced through our analysis. As such, the presence of TCS in the data set has not been definitively confirmed.

A histogram which would provide more well-defined separation between TCS and B-H events is that of the cross section ratio R = $\frac{2\int_0^{2\pi} d\phi \cos\phi \frac{dS}{dQ'^2 dt\, d\phi}}{\int_0^{2\pi} \frac{dS}{dQ'^2 dt\, d\phi}}$. The numerator and denominator of the ratio provide cross sections with and without the inclusion of a weight factor for the cos(ϕ) dependence of B-H data, meaning that the calculation of R would cause the B-H data function to flatten out in a histogram of R vs ϕ while TCS would remain a distinct sinusoidal function due to its $\cos(2\phi)$ dependence.

In the ratio R, the 'dS' term is an additional weighting term calculated from the equation $dS = \int_{\pi/4}^{3\pi/4} d\theta \frac{L(\theta,\phi)}{L_0(\theta)} \frac{d\sigma}{dQ'^2 dt\, d\theta\, d\phi}$, where the 'L' functions are weight factors relating to the scattering plane angles, invariant mass, and momenta for each detected event [3].

Due to the small statistical sample which we had to work with, for our calculation of R we would need to integrate over the invariant mass range, Q'^2, and the 4-momentum transfer from the proton before and after the proton-photon interaction, t, making use of the assumption that their values remain constant for TCS within the 2 – 3 GeV/c^2 range. With larger amounts of e^+e^- data, however, analyses may make use of non-fixed t values, which provide a function curve of R values rather than a single point to which the theoretically calculated GPD ratios for R may be compared.

Chapter 5: Conclusion and Future Work

5.1 Conclusion

Using the data provided by the GlueX Apparatus, we successfully identified the width variables σ_θ and σ_ϕ and $E_{\text{Preshower/Shower}}$ ratios of particle showers in the GlueX barrel calorimeter as the GlueX variables most sensitive to the differences between the ways in which e^+e^- and $\pi^+\pi^-$ interact within the detector. Using histograms to apply a series of five restrictions to these variables, we removed the $\pi^+\pi^-$ data, which was confirmed by the strengthening of the signal in the invariate mass histogram plots in the J/ψ meson mass region—where e^+e^- are known to be produced– with respect to the background data counts of primarily $\pi^+\pi^-$.

From the resulting data, we were able to transform the reaction into the rest frame of the e^+e^- particles, which allowed us to calculate the scattering plane angles of the particles with respect to the incoming particle plane, or production plane.

By removing events in the θ range in which B-H production occurs most prominently compared to TCS, we determined that differences in the cosine functions of the B-H and TCS reactions in our ϕ vs event count histogram were not possible to definitively confirm due to our limited statistics. As such, the presence of TCS in the dataset and the reaction's agreement with present GPD models, made possible through the calculation of R and its comparisons with theoretical GPD calculations of R, will depend on the preparation of an additional dataset to increase the size of the one which was utilized. The GlueX Experiment is in the process of generating a Spring 2018 dataset which would be an ideal resource with which to do so. The

application of the variable restrictions which I selected, coded, and utilized to this new combined data set would provide a useful point of continuation for this project.

5.2 Future Work

Future work or suggested improvements to this analysis could include an examination of pion data simulations to help to ensure that all $\pi^+\pi^-$ has been successfully removed. The use of 3-dimensional cuts, perhaps making use of the potential to probabilistically determine particle type differences with machine learning, could also more confidently ensure $\pi^+\pi^-$ removal. While we able to remove large amounts of pion data, our tight restrictions may have additionally reduced the e^+e^- sample size, so 3-D cuts could return these events to the dataset, allowing for stronger statistics for our ϕ dependence calculations.

Given a larger data set, it will be possible to determine the presence of TCS with more certainty, and to allow t and Q'^2 values to remain unfixed in our calculation of R, which will present more opportunities for its comparison to GPD parameters. With the ability to compare GPD models at multiple t values and plot them against R values, it may be possible to add additional parameters to the GPD proton structure models, improving their applicability to describing a larger variety of reactions and a more thorough picture of the proton structure.

Acknowledgements

I would like to sincerely thank my research advisor Professor Justin Stevens for his guidance and for always making time to share his extensive knowledge throughout my work on this project, and my academic advisor Professor Wouter Deconinck for his great encouragement and advice throughout my undergraduate semesters and for recommending this project to me.

I am also highly grateful to Jefferson Science Associates for generously aiding my research through the Minority/Female Undergraduate Research Assistantship, and to the GlueX Collaboration for all of the data I had the opportunity to work with!

Thank you also to Amy Schertz for allowing me to use her DSelector code to guide my Lorentz boost analysis, Alicia Remington and Zach Baldwin for their help answering my research questions, and the rest of the William and Mary GlueX Group for listening to and providing suggestions for my presentations.

I would also like to thank Professor Heather Sasinowska for agreeing to take part in my research committee and providing many useful suggestions, and Professor Irina Novikova for leading the committee and introducing me to my first physics research at William and Mary.

Appendices

The following contain excerpts of the code utilized in the methods and analysis of this project. The complete DSelector2_tcs.C script and its corresponding header file are located at https://github.com/jrstevenjlab/wm_gluex/tree/master/analysis/tcs/selector.

Appendix A-1:
Removal of pion data, after histogram and variable initializations

```
//Cut 1)
if ((locElectronSigThetaBCALShower > locElectronSigThetaCut) || (locPositronSigThetaBCALShower > locPositronSigThetaCut))
continue;
	dHist_Mee_ACcuts1->Fill(locMee);	//fills mass histogram with 1st cut implemented
	if(locMee > locMinJpsiMee && locMee < locMaxJpsiMee) {
		dHist_SigTheta_Preshower_JpsiACcuts1[0]->Fill(locElectronBCALPreshowerE, locElectronSigThetaBCALShower);
		dHist_SigTheta_Preshower_JpsiACcuts1[1]->Fill(locPositronBCALPreshowerE, locPositronSigThetaBCALShower);
	}
	else if(locMee > locMinBkgdMee && locMee < locMaxBkgdMee) {
		dHist_SigTheta_Preshower_BkgdACcuts1[0]->Fill(locElectronBCALPreshowerE, locElectronSigThetaBCALShower);
		dHist_SigTheta_Preshower_BkgdACcuts1[1]->Fill(locPositronBCALPreshowerE, locPositronSigThetaBCALShower);
	};


//Cut 2)
if ((locElectronBCALPreshowerE < 0.015) || (locPositronBCALPreshowerE < 0.015))  continue;
	dHist_Mee_ACcuts2->Fill(locMee);
	if(locMee > locMinJpsiMee && locMee < locMaxJpsiMee) {
		dHist_SigTheta_Preshower_JpsiACcuts2[0]->Fill(locElectronBCALPreshowerE, locElectronSigThetaBCALShower);
		dHist_SigTheta_Preshower_JpsiACcuts2[1]->Fill(locPositronBCALPreshowerE, locPositronSigThetaBCALShower);
	}
	else if(locMee > locMinBkgdMee && locMee < locMaxBkgdMee) {
		dHist_SigTheta_Preshower_BkgdACcuts2[0]->Fill(locElectronBCALPreshowerE, locElectronSigThetaBCALShower);
		dHist_SigTheta_Preshower_BkgdACcuts2[1]->Fill(locPositronBCALPreshowerE, locPositronSigThetaBCALShower);
	};


//Cut 3)
if ((locElectronSigThetaBCALShower > 0.025) || (locPositronSigThetaBCALShower > 0.025)) continue;
	dHist_Mee_ACcuts3->Fill(locMee);
	if(locMee > locMinJpsiMee && locMee < locMaxJpsiMee) {
		dHist_SigTrans_SigTheta_JpsiACcuts3[0]->Fill(locElectronSigThetaBCALShower, locElectronSigTransBCALShower);
		dHist_SigTrans_SigTheta_JpsiACcuts3[1]->Fill(locPositronSigThetaBCALShower, locPositronSigTransBCALShower);
	}
	else if(locMee > locMinBkgdMee && locMee < locMaxBkgdMee) {
		dHist_SigTrans_SigTheta_BkgdACcuts3[0]->Fill(locElectronSigThetaBCALShower, locElectronSigTransBCALShower);
		dHist_SigTrans_SigTheta_BkgdACcuts3[1]->Fill(locPositronSigThetaBCALShower, locPositronSigTransBCALShower);
	};
```

```
//Cut 4)
if ((locElectronEOverP < 0.75)|| (locPositronEOverP < 0.75)) continue;
		dHist_Mee_ACcuts4->Fill(locMee);
		if(locMee > locMinJpsiMee && locMee < locMaxJpsiMee) {
			dHistEOverP_Theta_BCAL_JpsiACcuts4[0]->Fill(locElectronTheta, locElectronEOverP);
			dHistEOverP_Theta_BCAL_JpsiACcuts4[1]->Fill(locPositronTheta, locPositronEOverP);
		}
		else if(locMee > locMinBkgdMee && locMee < locMaxBkgdMee) {
			dHistEOverP_Theta_BCAL_BkgdACcuts4[0]->Fill(locElectronTheta, locElectronEOverP);
			dHistEOverP_Theta_BCAL_BkgdACcuts4[1]->Fill(locPositronTheta, locPositronEOverP);
		};

//Cut 5)
if ((locElectronSigTransBCALShower > 0.013) || (locPositronSigTransBCALShower > 0.013)) continue;
		dHist_Mee_ACcuts5->Fill(locMee);
		if(locMee > locMinJpsiMee && locMee < locMaxJpsiMee) {
			dHist_SigTrans_SigTheta_JpsiACcuts5[0]->Fill(locElectronSigThetaBCALShower, locElectronSigTransBCALShower);
			dHist_SigTrans_SigTheta_JpsiACcuts5[1]->Fill(locPositronSigThetaBCALShower, locPositronSigTransBCALShower);
		}
		else if(locMee > locMinBkgdMee && locMee < locMaxBkgdMee) {
			dHist_SigTrans_SigTheta_BkgdACcuts5[0]->Fill(locElectronSigThetaBCALShower, locElectronSigTransBCALShower);
			dHist_SigTrans_SigTheta_BkgdACcuts5[1]->Fill(locPositronSigThetaBCALShower, locPositronSigTransBCALShower);
		};
```

Appendix A-2:
Transforming events' coordinate system with Lorentz boosts

```
//Boost 1:  (to gamma-p rest frame)
TLorentzVector loc_gpP4 = locBeamP4_Measured + dTargetP4;    // 4-momentum of photon & proton
TVector3 locGammap_boostvec = loc_gpP4.BoostVector();          // divide xyz momenta by time

TLorentzVector locBeamP4_gpRest = locBeamP4_Measured;    // copies/renames beam, to retain old axes
locBeamP4_gpRest.Boost(-1.0*locGammap_boostvec);           // boosts beam to gamma-p rest frame

TLorentzVector locElectronPositronP4_Measured = locElectronP4_Measured + locPositronP4_Measured;
//get sum of e+e- 4-momenta

TLorentzVector locElectronPositronP4_gpRest = locElectronPositronP4_Measured;  //  copy/rename lab e+e-
locElectronPositronP4_gpRest.Boost(-1.0*locGammap_boostvec);              //Lorentz boost e+e- into gp frame


//Boost 2:  (transform e+e- from gp to e+e- rest frame)
TVector3 locElectronPositron_boostvec = locElectronPositronP4_gpRest.BoostVector();
//dividing through by time for 3-vector
TLorentzVector locElectronPositronP4_eeRest = locElectronPositronP4_gpRest; // copy & rename e+e- rest 4p
locElectronPositronP4_eeRest.Boost(-1.0* locElectronPositron_boostvec);
// Lorentz boosting e+e- from gp into e+e- rest frame

TVector3 loc_eevec = locElectronPositronP4_eeRest.Vect();
 //coordinates vector needed to create locphi; contains x,y,z of e+e- plane vector

//transform proton momentum to e+e- rest frame in steps of the 2 boosts
TLorentzVector locProtonP4_ElectronPositronCM = locProtonP4_Measured;
locProtonP4_ElectronPositronCM.Boost(-1.0* locGammap_boostvec);
locProtonP4_ElectronPositronCM.Boost(-1.0* locElectronPositron_boostvec);
TVector3 locProtonP3_ElectronPositronCM = locProtonP4_ElectronPositronCM.Vect();

//Boost helicity (angular momentum projection) unit vectors to e+e- rest frame
TVector3 locHelicityZAxis_eeCM = -1.0*locProtonP3_ElectronPositronCM.Unit();
TVector3 locHelicityYAxis_eeCM = -1.0*locBeamP4_gpRest.Vect().Cross(locProtonP3_ElectronPositronCM).Unit();
TVector3 locHelicityXAxis_eeCM = locHelicityYAxis_eeCM.Cross(locHelicityZAxis_eeCM).Unit();

//Project the e+e- momentum onto these axes; allows theta & phi calculations
TVector3 loc_eeP3_Angles(loc_eevec.Dot(locHelicityXAxis_eeCM), loc_eevec.Dot(locHelicityYAxis_eeCM),
loc_eevec.Dot(locHelicityZAxis_eeCM));
```

Appendix A-3:
Creating the $cos(\theta)$ and ϕ histograms

(1)

```
//format & name histograms
dHist_cosThetavsPhi = new TH2F("cosThetavsPhi", ";Cos(theta) vs Phi", 600, -1.0, 1.0, 20, -1.0*TMath::Pi(),
1.0*TMath::Pi());
dHist_cosThetavsPhiLIM = new TH2F("cosThetavsPhiLIM", ";Cos(theta) vs Phi", 600, -1.0, 1.0, 20, -1.0*TMath::Pi(),
1.0*TMath::Pi());
dHist_phi = new TH1F("phi", ";phi (radians)", 600, -1.0*TMath::Pi(), 1.0*TMath::Pi());
dHist_phiLIM = new TH1F("phiLIM", ";phi (radians)", 600, -1.0*TMath::Pi(), 1.0*TMath::Pi());
//identical to phi but fill after setting cos(theta) range
```

(2)

```
        // initialize cos(theta), theta, & phi histogram variables
        double locphi = loc_eeP3_Angles.Phi();
        double loctheta = loc_eeP3_Angles.Theta();
        double loccostheta = loc_eeP3_Angles.CosTheta();
```

(3)

```
        if (locMee > 2 && locMee < 3){          //set mass range restriction
                dHist_cosThetavsPhi->Fill(loccostheta,locphi);
                if (locphi != 0){
                        dHist_phi ->Fill(locphi);
                        if ((loctheta > 0.25*TMath::Pi()) && (loctheta < 0.75*TMath::Pi() )){      //apply theta range
                            dHist_cosThetavsPhiLIM ->Fill(loccostheta,locphi);
                            dHist_phiLIM->Fill(locphi);
                        };
                };
        };
```

References

1. "Jefferson Lab Completes 12 GeV Upgrade". *Jefferson Lab*. Retrieved from: https://www.jlab.org/about
2. Berger, E.R., Diehl, M., Pire, B. (2002). "Timelike Compton scattering: exclusive photoproduction of lepton pairs." *The European Physical Journal C - Particles and Fields.* 23 (4), 675-689. Retrieved from https://arxiv.org/pdf/hep-ph/0110062.pdf.
3. Paremuzyan, R. (2010). "Timelike Compton Scattering" (Doctoral dissertation). Retrieved from https://www.jlab.org/Hall-B/general/thesis/Paremuzyan_thesis.pdf.
4. Mkrtchyan, A. "APS April Meeting 201." Jefferson Science Associates, LLC, 11 Apr. 2015, www.jsallc.org/IF/Reports/JSTF-2014-Mkrtchyan.pdf.
5. Goritschnig, A.T., Pire B.,Wagner J. (2014). "Timelike Compton scattering with a linearly polarized photon beam." *Physical Review D.* 89, 094031. Retrieved from https://journals.aps.org/prd/abstract/10.1103/PhysRevD.89.094031.
6. "The Standard Model: What Holds it Together: Quantum Mechanics". *The Particle Adventure: The Fundamentals of Matter and Force*. Lawrence Berkeley National Laboratory, 2014. Web. Retrieved from http://www.particleadventure.org/quantum_mech.html.
7. Griffiths, D. *Introduction to Quantum Mechanics*. Prentice Hall; 1st ed., 1994.
8. Moskowitz, C. "Proton Spin Mystery Gains a New Clue." *Scientific American*, 21 July 2014, www.scientificamerican.com/article/proton-spin-mystery-gains-a-new-clue1/.
9. Barbaro, M.B., Maieron, C., Voutier, E. "Lepton mass effects in the Bethe–Heitler process", *Physics Letters B*, vol. 726, Issues 1-3, 2013, pp. 505-511. Retrieved from https://www.sciencedirect.com/science/article/pii/S0370269313007028.
10. "List of accelerators in particle physics", Wikipedia, 2018. Retrieved from https://en.wikipedia.org/wiki/List_of_accelerators_in_particle_physics.
11. Al Ghoul, H. *et al*. "First Results from The GlueX Experiment", 2016. Retrieved from https://arxiv.org/pdf/1512.03699.pdf.

12. Al Ghoul, H. *et al*. "Measurement of the beam asymmetry Σ for π0 and η photoproduction on the proton at Eγ =9 GeV", 2017. Retrieved from https://arxiv.org/pdf/1701.08123.pdf.
13. Van Haarlem, Y. *et a*l. "The GlueX Central Drift Chamber: Design and Performance." *Nuclear Instruments & Methods in Physics Research Section A – Accelerators Spectrometers Detectors and Associated Equipment*, vol. 622, Issue 1, 2010, pp. 142-156. Retrieved from https://www.jlab.org/Hall-D/detector/CDC/construction/OnsiteReview/DOCS/cdc_nim_v2_5.pdf.
14. Stevens, J. "Gluonic Excitations and Experimental Hall-D at Jefferson Lab." PoS(DIS2014)239, 2014. *Proceedings of Science*, http://pos.sissa.it/203/239/pdf.
15. Ayala, A., Dominguez, C.A., Loewe, M., Zhang, Y. "Rho-meson resonance broadening in QCD at finite temperature." *Physical review D: Particles and fields*, vol. 86, Issue 11, 2012. Retrieved from https://www.researchgate.net/publication/232063577_Rho-meson_resonance_broadening_in_QCD_at_finite_temperature.
16. Beringer, J. *et al,* "Passage of Particles through Matter", 2013. Retrieved from http://pdg.lbl.gov/2013/reviews/rpp2013-rev-passage-particles-matter.pdf.